ETHzürich

CO2 Hydrogenation on Cu/Al2O3: Role of Metal/Support Interface in Driving Activity and Selectivity of a Bifunctional Catalyst

Journal Article

Author(s):
Lam, Erwin; Corral#Pérez, Juan J.; Larmier, Kim (ID); Noh, Gina (ID); Wolf, Patrick; Comas Vives, Aleix (ID); Urakawa, Atsushi; Copéret, Christophe (ID)

CO$_2$ Hydrogenation on Cu/Al$_2$O$_3$: Role of Metal/Support Interface in Driving Activity and Selectivity of a Bifunctional Catalyst

Erwin Lam[a], Juan José Corral-Pérez[b], Kim Larmier[a], Gina Noh[a], Patrick Wolf[a], Aleix Comas-Vives[a], Atsushi Urakawa[b], Christophe Copéret*,[a]

a]   ETH Zürich, Department of Chemistry and Applied Biosciences, Vladimir-Prelog-Weg 1-5, CH-8093, Zürich, Switzerland.

b]   Institute of Chemical Research of Catalonia (ICIQ), The Barcelona Institute of Science and Technology, 43007, Tarragona, Spain

1 Introduction

The hydrogenation of CO$_2$ into CH$_3$OH has been identified as a very promising route to mitigate the increasing anthropogenic CO$_2$ content in the atmosphere by incorporating CO$_2$ into a carbon-cycle, in the so-called methanol economy, provided that i) hydrogen is derived from green technology, e.g. water electrolysis using excess intermittent energy, and ii) efficient CO$_2$ capture technologies are available.[1-3] In that regard, copper-based catalysts are good candidates in terms of activity and selectivity for transforming CO$_2$ to CH$_3$OH.[1] However, the efficiency of the CO$_2$-to-CH$_3$OH synthesis can be significantly decreased by the competitive reverse-water-gas-shift (RWGS) reaction that transforms CO$_2$ into CO in addition to the thermodynamic limits of the reaction (~20% conversion at 230 °C and 30 bar). Among Cu-based catalysts, Cu/ZnO/Al$_2$O$_3$ and Cu/ZrO$_2$ have been shown to be effective in the selective hydrogenation of CO$_2$ to CH$_3$OH.[1, 4-11]

For Cu/ZrO$_2$, the selective CO$_2$ hydrogenation to CH$_3$OH is ascribed to Lewis acidic Zr(IV) surface sites, located at the periphery of Cu nanoparticles that facilitate the formation of formate and methoxy reaction intermediates.[12-13] For comparison, Cu/SiO$_2$ that does not contain Lewis acidic sites shows significantly lower activity and selectivity favoring CO formation. In fact, introducing surface Zr(IV) or Ti(IV) sites on SiO$_2$ at the interface with Cu nanoparticles via Surface Organometallic Chemistry (SOMC) increases the CH$_3$OH activity and selectivity, further supporting the importance of Lewis acid sites in this reaction.[13-14] Regarding CO, it has mainly been proposed to be formed on copper-based catalysts via two different mechanisms: The so-called redox and formate pathways. The former consists of the direct conversion of CO$_2$ to CO (that may involve M–COOH intermediates) and the subsequent reduction of Cu$_2$O surface species to Cu(0) metal forming H$_2$O, while the latter involves the

1

decomposition of formate into CO.[9, 15-27] Additionally, the formation of CO but also CH$_3$OH is often proposed to be related to the presence of oxygen defect sites originating from the oxide support.[28-36]

For Cu/ZnO/Al$_2$O$_3$, the origin of the promotional effect towards selective CH$_3$OH formation is still a matter of debate. For instance, CuZn alloy or the Cu/ZnO interface has been proposed to generate the active site responsible for the high CH$_3$OH selectivity.[37-44] In contrast, Al$_2$O$_3$, a minor component of the catalyst, is typically viewed as a stabilizing oxide that maintains the dispersion of Cu and Zn. However, considering the high reactivity of alumina toward many small molecules, including CH$_3$OH (vide infra),[45-48] e.g. the dehydration of CH$_3$OH to dimethyl ether (DME),[46] one may wonder about the involvement of alumina during the hydrogenation of CO$_2$. In fact, studies on CO$_2$ hydrogenation catalysts based on alumina-supported Cu nanoparticles are rare, and the influence of CH$_3$OH or the effect of the Lewis acidic support on activity/product selectivity are often overlooked.[15, 49-55]

In order to understand the role of alumina, we reasoned that studying alumina-supported Cu nanoparticles in the absence of zinc oxide would be ideal. We thus prepared small and narrowly dispersed Cu nanoparticles on Al$_2$O$_3$ via SOMC.[56-57] Using detailed catalytic studies augmented by ex-situ solid-state NMR, operando transient diffuse reflectance infrared spectroscopy (DRIFTS) and DFT modelling, we demonstrate that Cu/Al$_2$O$_3$ is a highly effective CO$_2$ hydrogenation catalyst in forming CH$_3$OH that is further converted into dimethyl ether (DME). We also show however that Cu/Al$_2$O$_3$ catalyzes the conversion of CO$_2$ to CO, and the formation and decomposition of methyl formate into CO, thus providing key information about the role of alumina in determining the selectivity in CO$_2$ hydrogenation.

2 Results and Discussion

2.1 Catalyst Synthesis and Characterization

Copper nanoparticles supported on alumina are prepared via SOMC[56] that involves grafting [Cu$_n$(Mesityl)$_n$] (n=2,4,5) in toluene on γ-alumina dehydroxylated at 500 °C (Al$_2$O$_3$-500, 2.1 OH nm$_{-2}$), followed by a reduction step under H$_2$ at 500 °C, yielding Cu$_{Xwt}$/Al$_2$O$_3$ where X specifies the Cu weight loading (Figure 1a). The copper loading is controlled by grafting a specific amount of [Cu$_n$(Mesityl)$_n$] (n=2,4,5) per nm$_2$ yielding catalysts with 2.4 and 3.8 wt% copper, referred to as Cu$_{2.4wt}$/Al$_2$O$_3$ and Cu$_{3.8wt}$/Al$_2$O$_3$, respectively (Table 1). After the grafting step, the IR spectrum shows the consumption of the surface Al-OH groups (bands above 3500 cm$_{-1}$) and the appearance of C-H stretching bands at around 3000 cm$_{-1}$ (Figure 1b and Figure A.1 for Cu$_{3.8wt}$/Al$_2$O$_3$). Subsequent treatment under H$_2$ at 500 °C restores the Al-OH groups

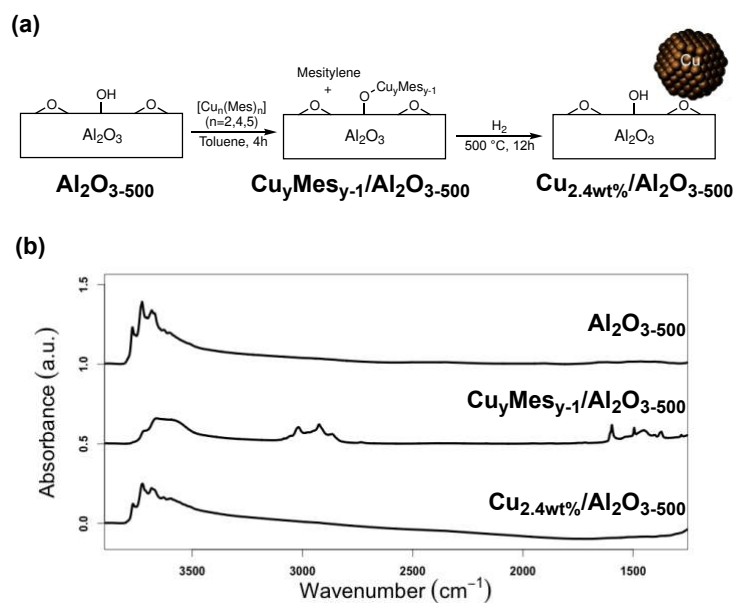while all C-H stretching bands disappear (Figure 1b), consistent with the removal of all organic ligands.

Figure 1. (a) Reaction scheme for the synthesis of copper nanoparticles on $Al_2O_{3\text{-}500}$ with a Cu loading of 2.4 wt% with Mes representing the mesitylene ligand. (b) IR spectra of grafting and reduction of $[Cu_n(Mesityl)_n]$ (n=2,4,5) on $Al_2O_{3\text{-}500}$.

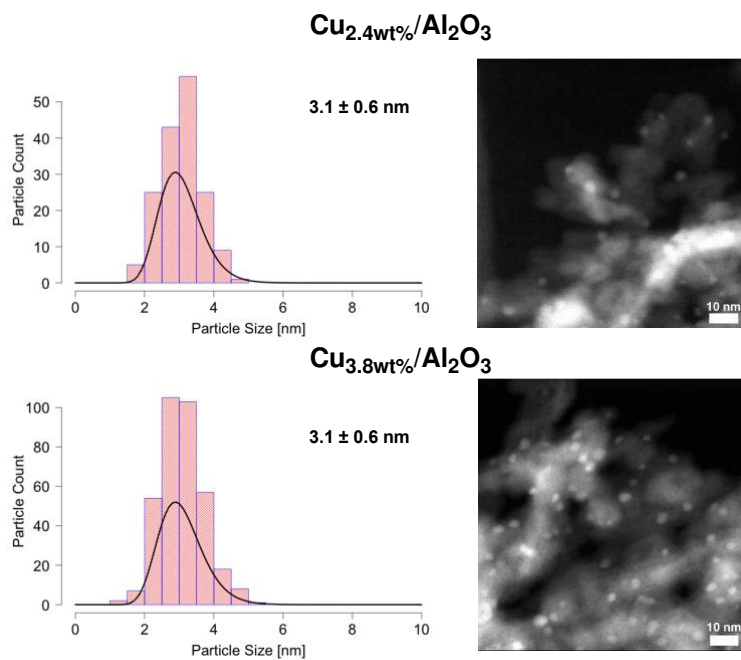**Figure 2.** HAADF-STEM and particle size distribution (particle counts > 150) of Cu_{xwt}/Al_2O_3 catalysts.

Dark-field scanning transmission electron microscopy indicates the formation of copper nanoparticles in both samples with sizes of 3.1 ± 0.6 nm for $Cu_{2.4wt\%}/Al_2O_3$ and $Cu_{3.8wt\%}/Al_2O_3$, respectively (Figure 2). The dispersal of copper particles takes place without the change in specific surface area that is ca. 140 m_2 g_{-1} according to N_2 adsorption/desorption isotherms (77 K) for both samples. In addition, powder X-ray diffraction shows only the crystalline phase of γ-Al_2O_3 and the absence of crystalline copper, consistent with the presence of small nanoparticles (Figure A.2). N_2O chemisorption shows that the copper surface site concentration is 40 μmol g_{cat-1} and 67 μmol g_{cat-1} for $Cu_{2.4wt}/Al_2O_3$ and $Cu_{3.8wt}/Al_2O_3$, respectively (Table 1), consistent with a similar particle size distribution by microscopy and dispersion by H_2 chemisorption (62 μmol g_{cat-1} and 86 μmol g_{cat-1} H_2 uptake for $Cu_{2.4wt\%}/Al_2O_3$ and $Cu_{3.8wt\%}/Al_2O_3$, respectively – Figure A.3), where a higher H_2 uptake is observed compared to N_2O. Overall using the methodology of grafting an organometallic precursor followed by reduction under H_2 leads to the formation of copper nanoparticles with similar dispersions, for both copper loadings.

Table 1. Physicochemical properties of copper-based catalysts.

Entry	Support	Cu content[a] [wt%]	Specific surface area[b] [m_2 g_{-1}]	Cu surface area based on N_2O[c] [μmol g_{cat-1}]	Cu surface area based on H_2[d] [μmol g_{cat-1}]	Particle size distribution[e] [nm]
1	$Cu/SiO_{2[f]}$	4.19	197	50/34	NA	2.9 ± 1.3
2	$Cu_{2.4wt\%}/Al_2O_3$	2.40	141	45/40	62	3.1 ± 0.6
3	$Cu_{3.8wt\%}/Al_2O_3$	3.81	139	66/67	86	3.1 ± 0.6

[a] Determined by ICP-OES; [b] Determined from N_2 physisorption applying the BET theory; [c] Measured on fresh/spent catalyst, assuming a 1:2 stoichiometry between N_2O and Cu surface sites; [d] Measured on fresh catalyst, assuming a 1:2 stoichiometry between H_2 and Cu surface sites [e] Determined by TEM on the fresh catalyst. [f] Reference [13].

2.2 Catalytic Studies

The thus-prepared catalysts were then evaluated in CO_2 hydrogenation in a fixed-bed flow reactor at 230 °C and 25 bar producing CH_3OH, CO and DME as the main products (Figure 2). Since DME is likely formed from the secondary reaction of CH_3OH on Al_2O_3 (vide infra),[46] we compare catalysts based on the combined formation rate of CH_3OH and DME (1:2

DME:CH₃OH stoichiometry), expressed in g CH₃OH g$_{Cu-1}$ h$_{-1}$. The catalysts are compared to the Cu/SiO₂ benchmark catalysts prepared via SOMC that also contain similar particles sizes according to TEM (Table 1).[13] The formation rates are given by extrapolation to 0 s g$_{cat}$ ml$_{-1}$ contact time (Figure A.4-A.8) from catalytic results reaching up to 7% conversion (Figure A.9). The equilibrium conversion under the given reaction conditions is around 17% including the dehydration of CH₃OH to DME and 15% without. For Cu$_{2.4wt\%}$/Al₂O₃ the intrinsic CH₃OH formation rate is around three times greater (0.89 g g$_{Cu-1}$ h$_{-1}$) than with Cu/SiO₂ (0.27 g g$_{Cu-1}$ h$_{-1}$), a non-Lewis acidic support. This increase in CH₃OH formation rate is paralleled by an increased intrinsic CO formation rate, of ca. four times (1.04 g g$_{Cu-1}$ h$_{-1}$) for Cu$_{2.4wt\%}$/Al₂O₃ compared to Cu/SiO₂. Increasing the Cu loading to 3.8 % (Cu$_{3.8wt\%}$/Al₂O₃) has hardly any effect on the intrinsic CH₃OH formation rate, while the CO formation rate decreases (0.73 g g$_{Cu-1}$ h$_{-1}$) (Figure 2). Overall, Cu/Al₂O₃ catalysts show higher formation rates for both CH₃OH and CO compared to Cu/SiO₂ while generating large amounts of DME that is not observed for Cu/SiO₂ as a result from the subsequent dehydration of CH₃OH on alumina.[46] While DME appears as a primary product as indicated by an intrinsic formation rate greater than zero; this is most likely due to strong adsorption of CH₃OH allowing the further dehydration to DME prior to desorption (vide infra). As proposed for Cu/ZrO₂ and related systems,[12-13] Lewis acidic supports likely promote the formation of CH₃OH, but stronger Lewis acids such as those found on Al₂O₃ are also able to further catalyze the dehydration of CH₃OH to DME.[46] Interestingly, Cu/Al₂O₃ also promotes CO formation, which is not observed for Cu/ZrO₂.[12] The CO and CH₃OH (including DME) formation rate decreases at higher conversions, i.e., longer contact time, consistent with the involvement of Lewis acidic sites and their inhibition by the coordination of reaction intermediates/products (Figure A.10-A.14). To further investigate the role (promotional effect) of Al₂O₃ on the observed selectivity patterns, in particular with respect to the increase of CO selectivity, not observed for Cu/ZrO₂, CO₂ hydrogenation was also investigated with physical mixtures of Cu/SiO₂ with varying amounts of Al₂O₃, while keeping the amount of copper constant. We note that Al₂O₃ in the absence of Cu does not shows any catalytic activity in CO₂ hydrogenation at 230 °C. The CO₂ hydrogenation carried out with a physical mixture consisting of a 5:1 (w/w) ratio of Cu/SiO₂:Al₂O₃ shows a similar formation rate for hydrogenated products (CH₃OH) as observed for Cu/SiO₂ but includes the formation of DME. In addition, the formation rate of CO is ca. doubled (0.49 g g$_{Cu-1}$ h$_{-1}$) by comparison with Cu/SiO₂, leading to an overall CO selectivity increase. Increasing the ratio of Al₂O₃ with Cu/SiO₂ to 1:1 (w/w) further increases the CO formation rate marginally (0.53 g g$_{Cu-1}$ h$_{-1}$), implying that a larger amount of Al₂O₃ does not further affect the rate determining step for CO

5

formation. The overall CH_3OH formation rate remains similar as found for Cu/SiO_2 with a rate of ca. 0.25 g g_{Cu-1} h-1 and a higher ratio for DME vs. CH_3OH (Figure 2). The same trends are observed when formation rates at higher conversions (1% and 2%) are considered, with the only observation being the decrease in formation rates for all the products due to product inhibition (Figure A.15). All the data are also recorded at conversions that are far away from equilibrium, with the catalytic reaction being kinetically controlled. Thus, Al_2O_3 is responsible for the increased formation rate of CO in the physical mixtures between Cu/SiO_2 and Al_2O_3, while it promotes both CO and CH_3OH formation rates in Cu/Al_2O_3 pointing out the role of interfacial sites in this reaction. In fact, for Cu_{Xwt}/Al_2O_3 (X = 2.4 and 3.8) samples (Figure 2), the CH_3OH formation rates are similar when normalized by the amount of copper due to having similar copper dispersions for both samples and the formation rate of CO decreases with higher copper loading but is proportional to the mass of the catalyst (Figure S16).
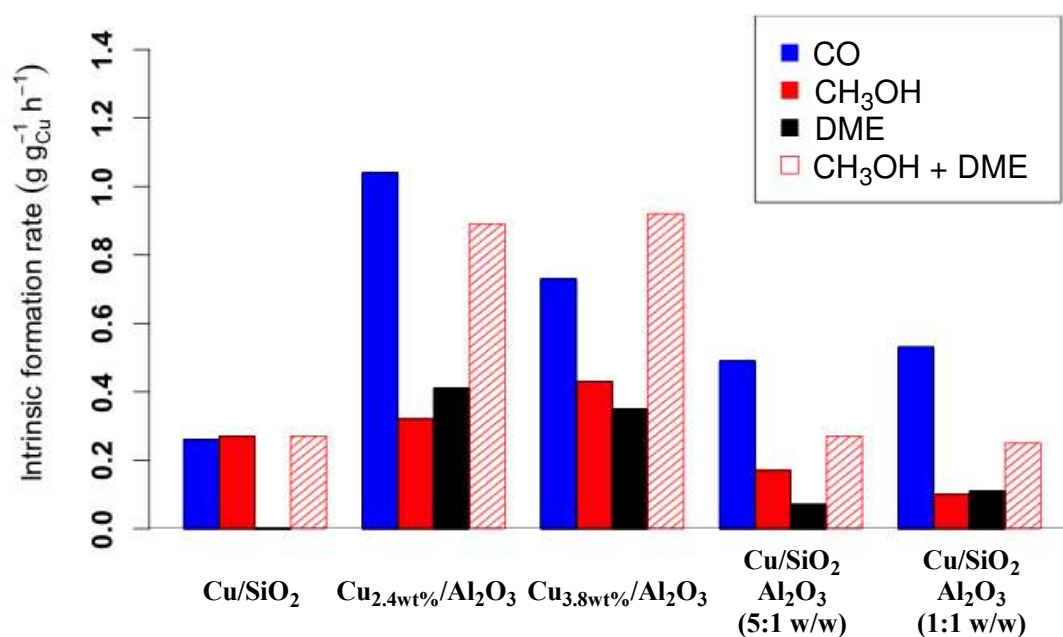

Figure 2. Intrinsic formation rates for Cu/SiO_2 and Cu/Al_2O_3 as well as physical mixtures of Cu/SiO_2 and Al_2O_3 for the formation of CO (blue), CH_3OH (red), DME (black) and overall CH_3OH formation (CH_3OH + DME red-dashed).

Since Al_2O_3 itself is not active for the RWGS reaction, these data also suggest that Al_2O_3 is able to mediate the formation of CO from products resulting from the hydrogenation of CO_2 on Cu/SiO_2. Plotting the ratio of CH_3OH with DME formation rates shows a clear correlation between the products, expected from DME originating from the dehydration of CH_3OH (Figure A.17). The ratio between CH_3OH and CO formation rates normalized by both the copper

loading and mass of catalyst does not show a clear correlation amongst different catalysts (Figure A.18-A.19), thus hinting to multiple reaction pathways for CO formation.

2.3 Mechanism for the Formation of Products and Byproducts – DME and CO – on Al_2O_3

In order to identify possible reaction intermediates formed on $Cu_{2.4wt\%}/Al_2O_3$, we used solid state NMR (Magic Angle Spinning (MAS) ^1H- and ^{13}C-ssNMR as well as ^1H-^{13}C HETCOR ssNMR after reaction with 5 bar of $^{13}CO_2$:$^1H_2$ (1:3 ratio) at 230 °C for 12 hours in a batch reactor (for details see Chapter A6), followed by evacuation of the gas phase at room temperature under high vacuum (10_{-5} mbar). The ^1H-^{13}C HETCOR spectrum shows the presence of two correlation peaks at 8/170 ppm and 2.9/48 ppm (Figure 3a), consistent with the formation of formate and methoxy species on the oxide support as previously observed on Cu/ZrO_2.[12-13] No adsorbed DME (expected at around 60 ppm in ^{13}C-ssNMR) is observed (Figure A.20), while both DME and CH_3OH are observed in the gas phase by ^{13}C solution NMR following the condensation of the gas phase after reaction in deuterated benzene (C_6D_6) (Figure 3b). The formation and desorption of DME is in fact also evidenced by transmission IR, where upon adsorption of 60 mbar of CH_3OH on Al_2O_3 and heating to 200 °C; the presence of H_2O and CH_3OH can be observed, but not adsorbed DME as evidenced by the absence of signals at around 1160 cm_{-1} (Figure A.21) which is only observed in the gas phase by NMR upon condensation of the gas phase in C_6D_6 (Figure A.22), showing that DME is more weakly adsorbed on the catalyst surface than other reaction intermediates and products such as CH_3OH or H_2O.[46] This is consistent with the strong adsorption of CH_3OH and the appearance of DME as a primary product generated by subsequent dehydration of CH_3OH.
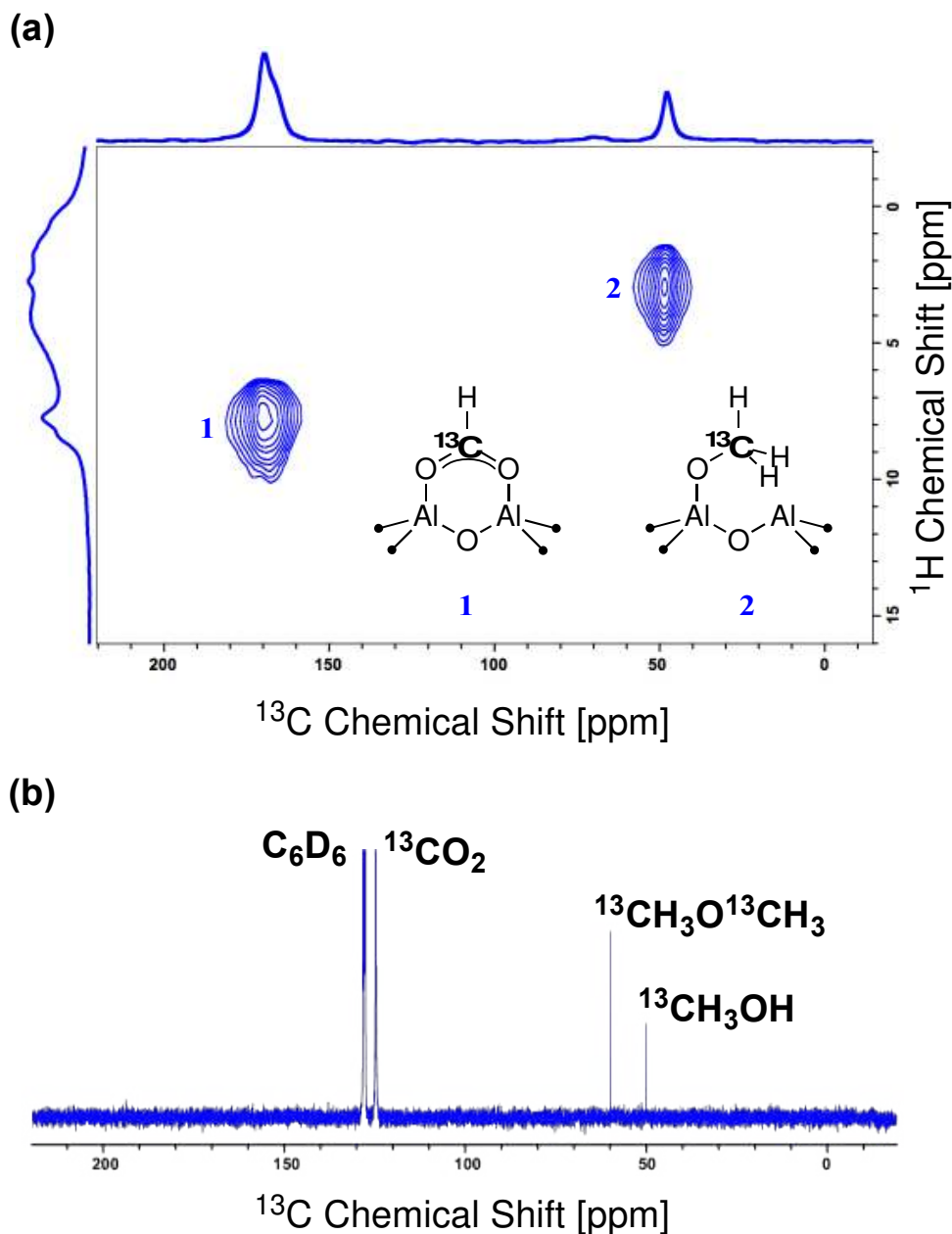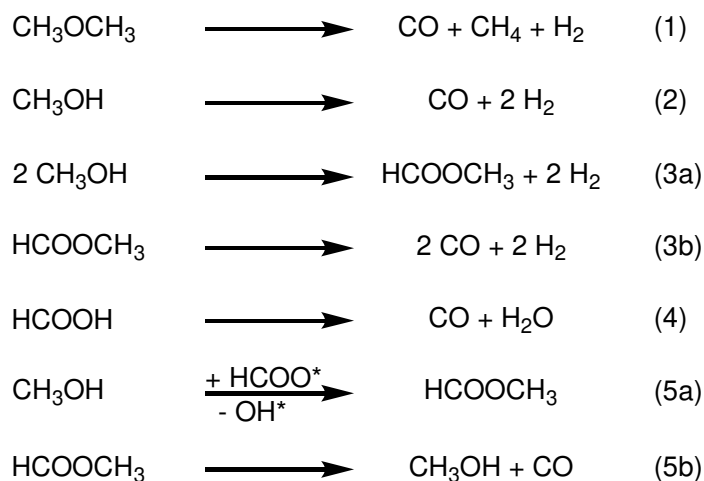
Figure 3. (a) Ex-situ MAS-NMR 1H -13C HETCOR spectra of Cu2.4wt%/Al2O3 reacted with CO2:H2 (1:3) at 5 bars for 12 hours and 230 °C. (b) Solution 13C NMR of the gas phase of Cu2.4wt%/Al2O3 after reaction recorded in C6D6.

CO can originate from several reaction pathways mediated by Al2O3. Among possible explanations, Al2O3 contains highly reactive surface sites able to activate small molecules that can mediate the formation of CO through the decomposition of DME/CH3OH or the formation and the subsequent decomposition of formic acid/methyl formate (Scheme 1).[47, 58] The decomposition of DME into CO requires concomitant formation of CH4 (eq. 1),[47] a product that is only observed in trace amounts under the investigated reaction conditions. Alternatively, the direct decomposition of CH3OH to CO (eq. 2) or the formation of methyl formate from two

8

equivalents of CH_3OH followed by decomposition to CO (eq. 3) are not likely either, due to a higher CO_2 conversion for the Cu/SiO_2 and Al_2O_3 physical mixtures. Similarly, the proposed decomposition of CH_3OH and methyl formate according to eq. 2 and 3 would lead to the formation of H_2, which is thermodynamically less likely considering the low conversion and since the use of high pressure of H_2 (15 bar) disfavor a reaction that generates H_2. CO could also arise from the decomposition of formic acid that can potentially be formed on Cu/SiO_2 and subsequently decomposes on Al_2O_3 to CO and H_2O (eq. 4).[21] It is for example known that formic acid can decompose to CO and H_2O on Al_2O_3 or SiO_2.[21] Finally, methyl formate formed upon reaction of CH_3OH with surface formate species (denoted as HCOO*) generating a surface hydroxyl group (OH*), could subsequently decompose to form CH_3OH and CO (eq. 5). In fact, surface formate species are observed by solid-state NMR upon reaction of the Cu/Al_2O_3 or Al_2O_3 with 5 bar of $_{13}CO_2:H_2$ (1:3) at 230 °C for 12 hours (Figure 3a and Figure A.23-A.24). The formation of methyl formate is known to occur during CO_2 hydrogenation at high pressures (300 bar) and can be further promoted by cofeeding CH_3OH,[59] but its decomposition is likely hindered at high pressures (300 bars).[49]

Scheme 1. Possible reaction pathways for the formation of CO.

$$CH_3OCH_3 \longrightarrow CO + CH_4 + H_2 \quad (1)$$

$$CH_3OH \longrightarrow CO + 2\ H_2 \quad (2)$$

$$2\ CH_3OH \longrightarrow HCOOCH_3 + 2\ H_2 \quad (3a)$$

$$HCOOCH_3 \longrightarrow 2\ CO + 2\ H_2 \quad (3b)$$

$$HCOOH \longrightarrow CO + H_2O \quad (4)$$

$$CH_3OH \xrightarrow[-\ OH^*]{+\ HCOO^*} HCOOCH_3 \quad (5a)$$

$$HCOOCH_3 \longrightarrow CH_3OH + CO \quad (5b)$$

Reaction of methyl formate with Al_2O_3 at 230 °C also yields CH_3OH, DME and CO, consistent with the decomposition of methyl formate into CH_3OH and CO at 230 °C with the concomitant dehydration of CH_3OH into DME under reaction conditions (Figure A.25). Furthermore, methyl formate is also shown to decompose to CO and CH_3OH on Cu/Al_2O_3 (Figure A.26).

In order to understand additional reaction pathways besides the decomposition of formic acid forming CO and H_2O on Al_2O_3 based catalyst,[15-16, 21] the effect of CH_3OH and its interaction with surface species for the formation of CO is further investigated. Thus, $Cu_{3.8wt\%}/Al_2O_3$ was studied by transient operando diffuse reflectance infrared spectroscopy (DRIFTS) with online activity monitoring to identify correlation between the gas phase composition with the concentrations of adsorbed intermediates. The changes in the IR spectrum and the gas phase composition are monitored at 230 °C and 5 bar under a transient condition, i.e. switching the atmosphere between a mixture of CO_2 and H_2 and a mixture of CO_2, H_2 and CH_3OH (vapor) (Figure 4a). In the latter atmosphere, concentrations of CH_3OH, DME, CO and methyl formate increased (Figure 4b and A.27), confirming that the formation of DME, CO and methyl formate are largely influenced by the concentration of CH_3OH. The IR spectrum in the region of 1000-1900 cm^{-1} shows two formate species that are behaving kinetically different (at ca. 1640 and 1670 cm^{-1}) based on multivariate curve resolution analysis.[60] The two formate species are proposed to be Al_2O_3 bound formates[16] and are quickly decreasing in intensity when CH_3OH is present (Figure 4c and A.28), in line with the rapid formation of methyl formate. In addition, when switching between CO_2/H_2 and Ar, the concentration of the formate species at ca. 1640 cm^{-1} is decreasing with a slower rate (Figure 4d blue), indicating that CH_3OH can indeed facilitate the removal/reaction of this surface formate species. This is further supported by a similar profile of the IR signals observed between 2500 and 3100 cm^{-1} corresponding to formate species (Figure A.29-A.30). In addition the evolution of methoxy species are shown in the region between 2500 and 3100 cm^{-1}: with a decrease in concentration of methoxy surface species when switching between $CO_2/H_2/CH_3OH$ and CO_2/H_2 (Figure A.29) vs. an increase in concentration of methoxy surface species when switching between Ar and CO_2/H_2 (Figure A.30). Overall, it shows the possible formation of methyl formate from CH_3OH that could then further decompose to CO on $Cu_{3.8wt\%}/Al_2O_3$.
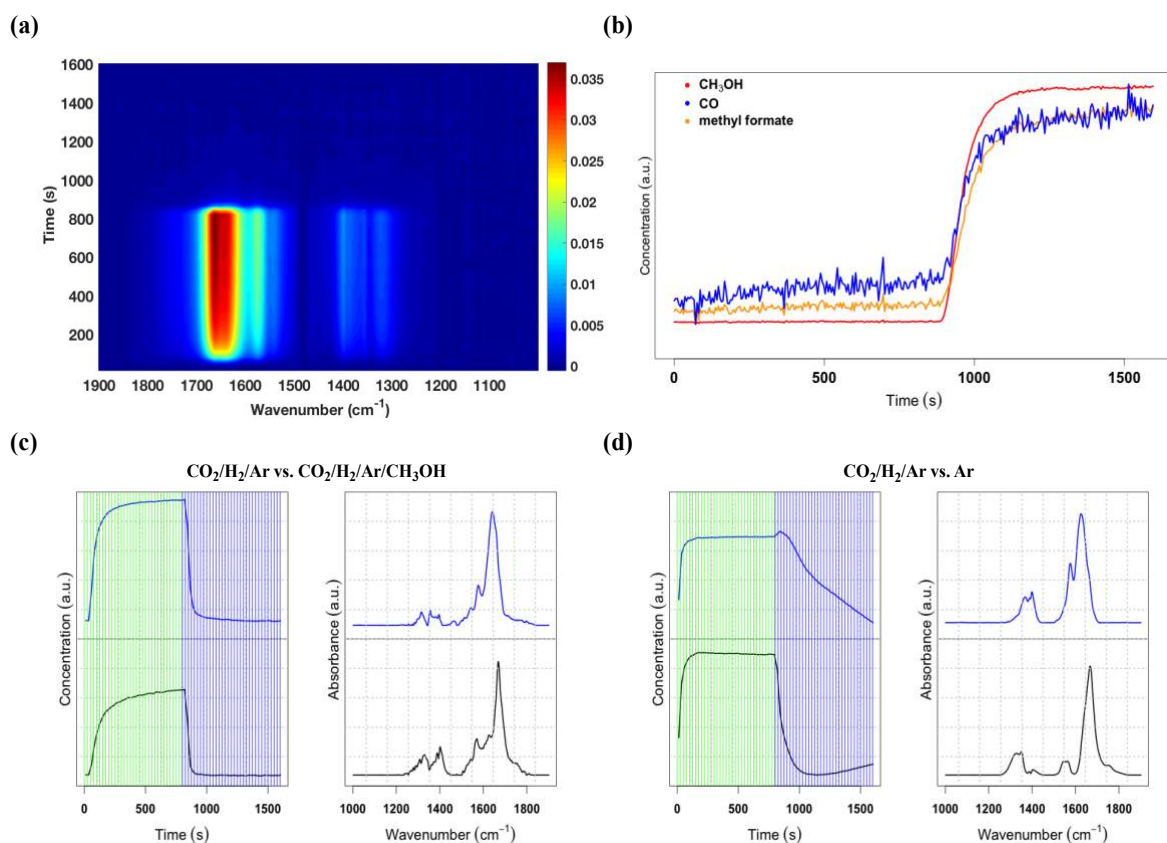
Figure 4. (a) Evolution of surface species between 1000 and 1900 cm-1 during transient operando DRIFTS experiments at 5 bar and 230 °C switching between $CO_2/H_2/Ar$ and $CO_2/H_2/Ar/CH_3OH$ for $Cu_{3.8\%}/A_2O_3$. (b) Gas phase concentration of CH_3OH, methyl formate and CO between gas mixtures of $CO_2/H_2/Ar$ and $CO_2/H_2/Ar/CH_3OH$. (c) (left) Concentration profile of two surface species (wavenumber 1000-1900 cm-1) corresponding to (right) component spectra in blue and black obtained by MCR analysis when switching between gas mixtures of $CO_2/H_2/Ar$ (green) and $CO_2/H_2/Ar/CH_3OH$ (blue). (d) (left) Concentration profile of two surface species (wavenumber 1000-1900 cm-1) corresponding to (right) component spectra in blue and black obtained by multivariate spectra analysis when switching between gas mixtures of $CO_2/H_2/Ar$ (green) and Ar (blue).

2.5 Role of the Metal/Oxide Interface on CH3OH and CO Formation

In order to obtain further information about the reaction mechanism, possible active site structures, and the role of perimeter sites around the copper nanoparticle, we investigated potential reaction pathways via a computational approach. The Cu/Al_2O_3 catalyst is modeled by placing a Cu_{67} particle (corresponding to ca. 1 nm diameter) on the most abundant (110)-facet of γ-Al_2O_3 (Figure 5a). This facet exposes different aluminum sites with different coordination number that can be found at the periphery (interface) between Cu and Al_2O_3. Due

to the copper nanoparticle size, the interface between the metal and the support can have various interfacial sites that are further investigated by DFT calculations. They are denoted **Al(III)**, **Al(IVA)** and **Al(IVB)**, the number indicating the coordination number and the letter describing two types of four-coordinated sites (Figure 5a).[45, 61] First, CO_2 can adsorb on these interfacial sites to generate bent monodentate (Figure 5b – **Al(III)**) or bridging (μ_2) CO_2 species by involving two neighboring aluminum sites (Figure 5b - **Al(III)-Al(IVB)** and **Al(IVA)-Al(IVA)**) with CO_2 adsorption free energy (calculated at 500 K) ranging from $\Delta_rG = -59$ to 63 kJ mol^{-1} (Figure 5b and Table A.1), while CO_2 does not interact with the Cu(111) surface and remains linear ($\Delta_rG = +46$ kJ mol^{-1}). This adsorbed CO_2 at the interface between copper and Al_2O_3 can then further react with surface Cu-hydrides generated by splitting H_2 on the copper particle forming CH_3OH or CO (Figure 5c, Figure A.31-A.32 and Table A.2), similar to the pathway proposed by DFT calculation for Cu/ZrO_2.[12] CO_2 is hydrogenated to formate (HCOO*), acetal (CH$_2$OO*) and (CH$_2$OOH*) upon which the C-O bond is broken forming CH$_2$O* and OH*. Further hydrogenation yields methoxy (CH$_3$O*) and hydroxide (OH*) (Figure 5c) and finally CH_3OH and H_2O that can desorb from the catalyst, closing the catalytic cycle. Alternatively, the CO_2 adsorbed at the interface of the copper nanoparticle and Al_2O_3 can directly split into CO* and O* (Figure 5b). The O* is located at the interface between copper and Al_2O_3 while CO coordinated on copper that desorbs. Further hydrogenation yields H_2O that desorbs from the catalyst, similar to what was shown on Ni/Al_2O_3, where the interfacial sites are playing a key role during the RWGS reaction.[62-63]
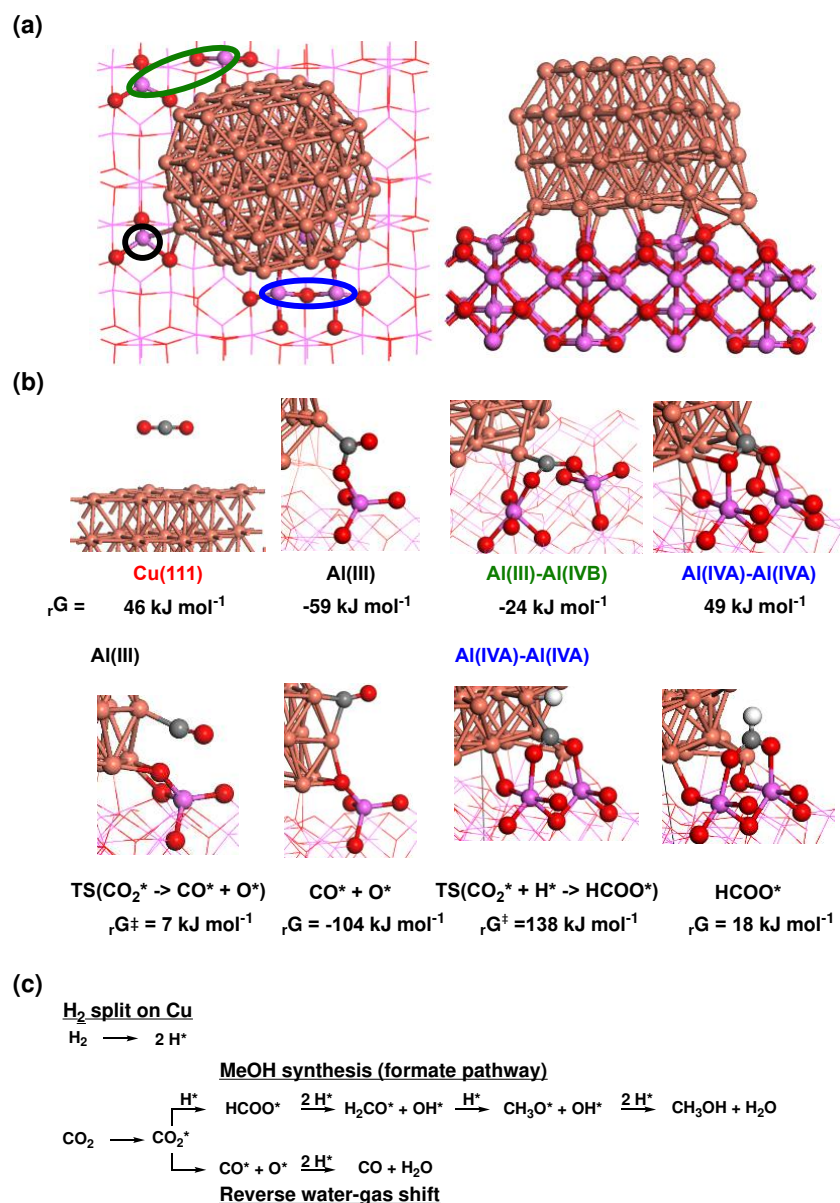
Figure 5. (a) Top (left) and side (right) view of the computational model consisting of the (110) facet of γ-Al$_2$O$_3$ and a Cu$_{67}$ particle with the aluminum interfacial sites circled for **Al(III)** (black), **Al(III)-Al(IVB)** (green) and **Al(IVA)-Al(IAV)** (blue). (b) Structure and adsorption free energy (Δ$_r$G) calculated at 500 K in kJ mol^{-1} of CO$_2$ interacting with the **Cu(111)** facet and the interfacial sites with respect to gas phase CO$_2$. **Al(III)** site (black circle), an **Al(III)** site in close proximity to an **Al(IVB)** site (green circle), and two **Al(IVA)** sites in close proximity (blue circle). Transition state for the formation of CO* + O* and HCOO* on **Al(III)** and **Al(IV)-Al(IV)**, respectively. (c) Reaction mechanism for the formation of Cu-H, CH$_3$OH via the formate pathway, and CO.

13

Overall, sites where CO_2 is coordinated in a monodentate geometry as on **Al(III)** appears to favor CO formation, whereas CO_2 adopting a bridging (μ_2) coordination favors the formation of HCOO* and ultimately CH_3OH on **Al(IVA)-Al(IVA)**. Thus, depending on the nature of the aluminum site it can either favor CH_3OH or CO. This can be explained by the geometry of CO_2 (Figure 5b). Bonding in a monodentate geometry allows to easily break the C-O bond leading to the RWGS reaction being favored, while having a bridging (μ_2) coordination CO_2* consist of a geometry that resembles this of formate species (HCOO*), hence the low activation barrier for its formation. It shows that CO_2 hydrogenation at the Cu/Al_2O_3 interface lowers the activation energy for both CH_3OH and CO in comparison to the **Cu(111)** surface (for further details see Chapter A6). This is consistent with the increase in CH_3OH and CO formation rate found experimentally and in line with the inhibition for both the CH_3OH and CO formation at longer contact times due to coordination on Lewis acid sites by reaction products (H_2O/CH_3OH) that have a stronger adsorption energy than CO_2. The formation of DME is shown not to require the presence of copper and can solely take place on the Al_2O_3 surface, where by DFT calculation, DME is preferentially formed on more strongly Lewis acidic sites (Scheme A.1). In addition, the most strongly adsorbed reaction intermediates determined by DFT calculation (HCOO* and CH_3O*) are the same intermediates observed with ex situ solid state NMR experiments (vide supra).

3 Conclusion

Copper nanoparticles (2-4 nm) supported on Al_2O_3 is a bifunctional catalyst that is particularly active toward the catalytic hydrogenation of CO_2 into CH_3OH, DME and CO, in contrast to what is observed with SiO_2 or ZrO_2 supports that show low activity and selectivity or promote only CH_3OH formation rate, respectively. The formation of CH_3OH and CO as well as the further dehydration of CH_3OH to DME is due to the strongly Lewis acidic Al_2O_3 support that promotes both of these reactions. The observed promotional effect is traced back to specific interfacial sites present between copper and Al_2O_3, that favors CH_3OH formation via formate intermediates, but also the direct conversion of CO_2 to CO. In addition, these Lewis acid sites open additional reaction pathways, converting surface formate intermediates upon reaction with CH_3OH to methyl formate that can then further decompose into CO. This study thus showcases how the Al_2O_3 support can participate in the formation of a broad range of products, increasing both CH_3OH and CO production rates and also helps rationalizing the effect of Lewis acidic oxide supports on the catalytic properties of Cu nanoparticles in CO_2 hydrogenation. Such

information provides guidelines on ways to tune the catalytic performances of CO_2 hydrogenation catalysts that we are currently exploring.

4 Experimental Section

General: SiC (FisherEU) and CH_3OH (Acros Chemicals) were used as received. Pentane and toluene were purified over two solvent purification alumina columns (MBraun) and degassed prior to use. Methyl formate (Acros Chemicals) was distilled over P_2O_5 and degassed. H_2 for catalyst preparation was purified over activated R3-11 BASF catalyst and activated 4 Å molecular sieves. Al_2O_3 (TH 100/150) was provided from Sasol and calcined at 500 °C under synthetic air, followed by evacuation under high vacuum and stored in an argon filled glovebox (denoted as Al_2O_{3-500}). Unless otherwise specified all preparations of catalysts were carried out under argon using standard Schlenk techniques and gloveboxes. [Cu_n(Mesitylene)$_n$][64] and Cu/SiO_2[13] were synthesized according to literature procedures and stored in an argon filled glovebox. All the details concerning material characterization and catalytic testing are described in chapter 2,3 and 4.

Representative procedure for supported copper nanoparticle synthesis: A solution of [Cu_n(Mesitylene)$_n$] (220 mg, 0.24 mmol (for n = 5)) in 20 mL of toluene was added to 2 g of the Al_2O_3 dehydroxylated at 500 °C wetted with toluene. The suspension was stirred for 4 hours, washed three times with toluene (5 mL) and dried at 10^{-5} mbar for 1 hour. The solid was then reduced under H_2 at 500 °C for 5 hours (100 °C h$_{-1}$) cooled down to room temperature under H_2, evacuated under high vacuum (10^{-5} mbar) and stored in an argon filled glovebox. Grafting on a NMR scale using ferrocene as internal standard, shows the release of 0.4 equiv. mesitylene and maximal consumption of 0.24 equiv. [Cu_n(Mesitylene)$_n$] (for n = 5) with respect to the OH density (0.52 mmol/g), in line with the maximum Cu loading of 3.8 wt%.

Procedure for methanol dehydration: A self-supporting pellet of Al_2O_{3-500} in a reactor equipped with CaF_2 windows were contacted with 60 mbar of CH_3OH and heated to 200 °C for 30 min after which the IR spectrum of the pellet was recorded. Reference spectra of Al_2O_{3-500} and Al_2O_{3-500} contacted with DME (30 mbar) were recorded in the same fashion.

Representative procedure for methyl formate decomposition: To 50 mg of catalyst in a volume of 15 cm$_3$ was introduced 60 mbar of methyl formate and heated to 230 °C using a sand bath (300 °C/h). The gas phase was analyzed by GC before heating, after 30 minutes while heating and 2 hours after the start of the experiment.

4.1 Transient DRIFTS and MCR Analysis

The samples were ground to fine powders and placed in a custom-made reaction cell with a ZnSe window that allowed to pressurize the system to 5 bar. The material was then reduced under a stream of H_2 at 300 °C for 1 hour. Transient DRIFTS studies were then performed by switching two different reactant gases (Ar, Ar/CH_3OH, CO_2/H_2/Ar (1:3 ratio CO_2:H_2 with 4% Ar) or CO_2/H_2/Ar/CH_3OH) that periodically flow through the catalyst as previously reported.[59] For the gases containing CH_3OH, the gases were passed through a saturator containing CH_3OH at room temperature. Transient experiments were performed at 230 °C and 5 bar by periodically changing between two stream of gases every 800 s, to obtain four cycles (4 x 1600s). The products were analyzed using a mass spectrometer (OmniStar GSD 320 O series, Pfeiffer Vacuum) or by transmission IR (ALPHA IR spectrometer, Bruker) in *operando* studies. The last three cycles were averaged to enhance the signal to noise ratio. Multivariate spectral analysis was performed by means of multivariate curve resolution (MCR) as described elsewhere.[60]

4.2 Computational Details

Periodic DFT calculations were carried out with Vienna Ab Initio Simulation Package (VASP) code[65-67] using the projector augmented wave (PAW) method with a plane wave energy cutoff of 400 eV and the PBE exchange-correlation functional.[68] The criterion convergence chosen for the SCF cycle was 10^{-5} eV, and optimizations were considered converged once the forces on all atoms were lower than 0.1 eV.$Å^{-1}$. To model the alumina surface, we considered a slab of the (110) termination of γ-alumina. The slab was 16.1 x 16.8 Å large, and 5 Å thick (144 atoms, 32 Al_2O_3 units), with a vacuum separation of ca 15 Å. The two lowest atomic layers were frozen during optimizations and transition state calculations. The Brillouin zone was sampled with a 3 x 3 x 1 k-point grid. Electron occupancies were determined according to a gaussian scheme with an energy smearing of 0.1 eV. For the supported copper particle, a Cu_{67} cluster of half-truncated octahedron shape from Cu fcc structure was deposited on the surface. The Cu/Al_2O_3 model was optimized before studying the adsorption and reactivity of CO_2 and H_2. Cu(111) was simulated using a periodic 3 x 3 four-layer slab consisting of 36 Cu atoms with a vacuum separation of 15 Å. During optimization, the bottom Cu(111) layer was frozen. The Brillouin zone was sampled with a 3 x 3 x 1 k-point grid. Electron occupancies were determined according to a Methfessel-Paxton scheme with an energy smearing of 0.2 eV. In order to correct for errors in the gas-phase thermochemistry, the energy of the gas phase CO was reduced by 50 kJ/mol.[62] Transition states were determined using the Climbing Image

Nudge Elastic Band (Cl-NEB) method[69] with 8 images and were confirmed by the presence of a single negative mode in frequency analysis. Thermodynamic calculations were performed by including enthalpic and entropic contributions to obtain the Gibbs free energies at 500 K from vibrational frequencies from gas-phase, adsorbed species and transition states reported elsewhere.[12] The term $\Delta_r G$ corresponds to the relative free energy between the adsorbed molecule or reaction intermediate and the term $\Delta_r G_{\ddagger}$ corresponds to the relative free energy of the transition state with respect to the free energy of CO_2 and H_2 in the gas phase and Cu/Al_2O_3.

5 References

[1]   A. Álvarez, A. Bansode, A. Urakawa, A. V. Bavykina, T. A. Wezendonk, M. Makkee, J. Gascon, F. Kapteijn, *Chem. Rev.* **2017**, *117*, 9804-9838.

[2]   G. Olah, A. Goeppert, S. G. K. Prakash, *Beyond Oil and Gas: The Methanol Economy, 2nd ed.*, Wiley-VCH: Weinheim, Germany, **2011**.

[3]   A. Olah George, *Angew. Chem., Int. Ed.* **2012**, *52*, 104-107.

[4]   K. T. Jung, A. T. Bell, *Catal. Lett.* **2002**, *80*, 63-68.

[5]   J. Weigel, R. A. Koeppel, A. Baiker, A. Wokaun, *Langmuir* **1996**, *12*, 5319-5329.

[6]   A. Baiker, M. Kilo, M. Maciejewski, S. Menzi, A. Wokaun, in *Stud. Surf. Sci. Catal.* **1993**, *75*, 1257-1272.

[7]   C. Schild, A. Wokaun, A. Baiker, *J. Mol. Catal.* **1990**, *63*, 243-254.

[8]   S. Tada, K. Larmier, R. Buchel, C. Coperet, *Catal. Sci. Technol.* **2018**, *8*, 2056-2060.

[9]   Y. Amenomiya, *J. Catal.* **1979**, *57*, 64-71.

[10]   E. Ramaroson, R. Kieffer, A. Kiennemann, *Appl. Catal.* **1982**, *4*, 281-286.

[11]   J. Schumann, T. Lunkenbein, A. Tarasov, N. Thomas, R. Schlögl, M. Behrens, *ChemCatChem* **2014**, *6*, 2889-2897.

[12]   K. Larmier, W. C. Liao, S. Tada, E. Lam, R. Verel, A. Bansode, A. Urakawa, A. Comas-Vives, C. Copéret, *Angew. Chem., Int. Ed.* **2017**, *56*, 2318-2323.

[13]   E. Lam, K. Larmier, P. Wolf, S. Tada, O. V. Safonova, C. Copéret, *J. Am. Chem. Soc.* **2018**, *140*, 10530-10535.

[14]   G. Noh, E. Lam, J. L. Alfke, K. Larmier, K. Searles, P. Wolf, C. Copéret, *ChemSusChem* **2019**, *12*, 968-972.

[15]   C.-S. Chen, W.-H. Cheng, S.-S. Lin, *Catal. Lett.* **2000**, *68*, 45-48.

[16]   N. Ishito, K. Hara, K. Nakajima, A. Fukuoka, *J. Energy Chem.* **2016**, *25*, 306-310.

[17]   G. Jacobs, A. C. Crawford, B. H. Davis, *Catal. Lett.* **2005**, *100*, 147-152.

[18]   T. van Herwijnen, W. A. de Jong, *J. Catal.* **1980**, *63*, 83-93.

[19] T. van Herwijnen, R. T. Guczalski, W. A. de Jong, *J. Catal.* **1980**, *63*, 94-101.

[20] J. F. Edwards, G. L. Schrader, *J. Phys. Chem.* **1984**, *88*, 5620-5624.

[21] Y. Noto, K. Fukuda, T. Onishi, K. Tamaru, *Trans. Faraday Soc.* **1967**, *63*, 2300-2308.

[22] A. A. Gokhale, J. A. Dumesic, M. Mavrikakis, *J. Am. Chem. Soc.* **2008**, *130*, 1402-1414.

[23] D. Tibiletti, A. Goguet, F. C. Meunier, J. P. Breen, R. Burch, *Chem. Commun.* **2004**, 1636-1637.

[24] G. Jacobs, B. H. Davis, *Appl. Catal., A* **2005**, *284*, 31-38.

[25] R. Zhang, B. Wang, H. Liu, L. Ling, *J. Phys. Chem. C* **2011**, *115*, 19811-19818.

[26] D. C. Grenoble, M. M. Estadt, D. F. Ollis, *J. Catal.* **1981**, *67*, 90-102.

[27] E. L. Kunkes, F. Studt, F. Abild-Pedersen, R. Schlögl, M. Behrens, *J. Catal.* **2015**, *328*, 43-48.

[28] D. Ferri, T. Bürgi, A. Baiker, *Phys. Chem. Chem. Phys.* **2002**, *4*, 2667-2672.

[29] Y. A. Daza, J. N. Kuhn, *RSC Adv.* **2016**, *6*, 49675-49691.

[30] S. S. Kim, H. H. Lee, S. C. Hong, *Appl. Catal., A* **2012**, *423-424*, 100-107.

[31] L. F. Bobadilla, J. L. Santos, S. Ivanova, J. A. Odriozola, A. Urakawa, *ACS Catal.* **2018**, *8*, 7455-7467.

[32] T. Jin, Y. Zhou, G. J. Mains, J. M. White, *J. Phys. Chem.* **1987**, *91*, 5931-5937.

[33] C. M. Kalamaras, S. Americanou, A. M. Efstathiou, *J. Catal.* **2011**, *279*, 287-300.

[34] A. Goguet, F. C. Meunier, D. Tibiletti, J. P. Breen, R. Burch, *J. Phys. Chem. B* **2004**, *108*, 20240-20246.

[35] K. Sun, M. Kohyama, S. Tanaka, S. Takeda, *J. Phys. Chem. C* **2017**, *121*, 12178-12187.

[36] K. Samson, M. Śliwa, R. P. Socha, K. Góra-Marek, D. Mucha, D. Rutkowska-Zbik, J. F. Paul, M. Ruggiero-Mikołajczyk, R. Grabowski, J. Słoczyński, *ACS Catal.* **2014**, *4*, 3730-3741.

[37] M. Behrens, F. Studt, I. Kasatkin, S. Kühl, M. Hävecker, F. Abild-Pedersen, S. Zander, F. Girgsdies, P. Kurr, B.-L. Kniep, M. Tovar, R. W. Fischer, J. K. Nørskov, R. Schlögl, *Science* **2012**, *336*, 893.

[38] T. Fujitani, I. Nakamura, T. Uchijima, J. Nakamura, *Surf. Sci.* **1997**, *383*, 285-298.

[39] C. Tisseraud, C. Comminges, T. Belin, H. Ahouari, A. Soualah, Y. Pouilloux, A. Le Valant, *J. Catal.* **2015**, *330*, 533-544.

[40] A. Le Valant, C. Comminges, C. Tisseraud, C. Canaff, L. Pinard, Y. Pouilloux, *J. Catal.* **2015**, *324*, 41-49.

[41]   J. D. Grunwaldt, A. M. Molenbroek, N. Y. Topsøe, H. Topsøe, B. S. Clausen, *J. Catal.* **2000**, *194*, 452-460.

[42]   S. Kuld, M. Thorhauge, H. Falsig, C. F. Elkjær, S. Helveg, I. Chorkendorff, J. Sehested, *Science* **2016**, *352*, 969.

[43]   T. Lunkenbein, J. Schumann, M. Behrens, R. Schlögl, M. G. Willinger, *Angew. Chem., Int. Ed.* **2015**, *54*, 4544-4548.

[44]   S. Kuld, C. Conradsen, P. G. Moses, I. Chorkendorff, J. Sehested, *Angew. Chem., Int. Ed.* **2014**, *53*, 5941-5945.

[45]   R. Wischert, P. Laurent, C. Copéret, F. Delbecq, P. Sautet, *J. Am. Chem. Soc.* **2012**, *134*, 14430-14449.

[46]   R. S. Schiffino, R. P. Merrill, *J. Phys. Chem.* **1993**, *97*, 6425-6435.

[47]   A. Comas-Vives, M. Valla, C. Copéret, P. Sautet, *ACS Cent. Sci.* **2015**, *1*, 313-319.

[48]   G. Busca, P. F. Rossi, V. Lorenzelli, M. Benaissa, J. Travert, J. C. Lavalley, *J. Phys. Chem.* **1985**, *89*, 5433-5439.

[49]   A. Bansode, B. Tidona, P. R. von Rohr, A. Urakawa, *Catal. Sci. Technol.* **2013**, *3*, 767-778.

[50]   T. Hyakutake, W. van Beek, A. Urakawa, *J. Mater. Chem. A* **2016**, *4*, 6878-6885.

[51]   K. K. Bando, K. Sayama, H. Kusama, K. Okabe, H. Arakawa, *Appl. Catal., A* **1997**, *165*, 391-409.

[52]   H. Ren, C.-H. Xu, H.-Y. Zhao, Y.-X. Wang, J. Liu, J.-Y. Liu, *J. Ind. Eng. Chem.* **2015**, *28*, 261-267.

[53]   J. B. Wang, H.-K. Lee, T.-J. Huang, *Catal. Lett.* **2002**, *83*, 79-86.

[54]   V. N. Ipatieff, G. S. Monroe, *J. Am. Chem. Soc.* **1945**, *67*, 2168-2171.

[55]   T. Tagawab, G. Pleizier, Y. Amenomiya, *Appl. Catal.* **1985**, *18*, 285-293.

[56]   C. Copéret, A. Comas-Vives, M. P. Conley, D. P. Estes, A. Fedorov, V. Mougel, H. Nagae, F. Núñez-Zarur, P. A. Zhizhko, *Chem. Rev.* **2016**, *116*, 323-421.

[57]   C. Copéret, F. Allouche, K. W. Chan, M. P. Conley, M. F. Delley, A. Fedorov, I. B. Moroz, V. Mougel, M. Pucino, K. Searles, K. Yamamoto, P. A. Zhizhko, *Angew. Chem., Int. Ed.* **2018**, *57*, 6398-6440.

[58]   A. Y. Rozovskii, G. I. Lin, *Top. Catal.* **2003**, *22*, 137-150.

[59]   J. J. Corral-Pérez, A. Bansode, C. S. Praveen, A. Kokalj, H. Reymond, A. Comas-Vives, J. VandeVondele, C. Copéret, P. R. von Rohr, A. Urakawa, *J. Am. Chem. Soc.* **2018**, *140*, 13884-13891.

[60]   A. de Juan, J. Jaumot, R. Tauler, *Anal. Methods* **2014**, *6*, 4964-4976.

[61]   M. Digne, P. Sautet, P. Raybaud, P. Euzen, H. Toulhoat, *J. Catal.* **2002**, *211*, 1-5.

[62]   L. Foppa, T. Margossian, S. M. Kim, C. Müller, C. Copéret, K. Larmier, A. Comas-Vives, *J. Am. Chem. Soc.* **2017**, *139*, 17128-17139.

[63]   M.-C. Silaghi, A. Comas-Vives, C. Copéret, *ACS Catal.* **2016**, *6*, 4501-4505.

[64]   E. M. Meyer, S. Gambarotta, C. Floriani, A. Chiesi-Villa, C. Guastini, *Organometallics* **1989**, *8*, 1067-1079.

[65]   G. Kresse, J. Furthmüller, *Comput. Mater. Sci.* **1996**, *6*, 15-50.

[66]   G. Kresse, J. Hafner, *Phys. Rev. B* **1993**, *47*, 558-561.

[67]   G. Kresse, J. Hafner, *Phys. Rev. B* **1994**, *49*, 14251-14269.

[68]   J. P. Perdew, J. A. Chevary, S. H. Vosko, K. A. Jackson, M. R. Pederson, D. J. Singh, C. Fiolhais, *Phys. Rev. B* **1992**, *46*, 6671-6687.

[69]   G. Henkelman, B. P. Uberuaga, H. Jónsson, *J. Chem. Phys.* **2000**, *113*, 9901-9904.